J Mater Sci (2011) 46:6235–6242
DOI 10.1007/s10853-010-4972-8

ABBASCHIAN FESTSCHRIFT

Phase quantification of impulse atomized $Al_{68.5}Ni_{31.5}$ alloy

A. Ilbagi · H. Henein · A. B. Phillion

Received: 19 June 2010 / Accepted: 4 October 2010 / Published online: 2 November 2010

Abstract Powders of $Al_{68.5}Ni_{31.5}$ were produced using the impulse atomization technique. The molten droplets were cooled in-flight by the stagnant helium or nitrogen in the atomizing chamber, and the resulting powders were sieved into different size ranges. Scanning electron microscopy, X-ray diffraction, and neutron diffraction were used in order to study the microstructure and to quantify the phase fractions in the samples. The computer software GSAS was used to calculate the weight fraction of the existing phases, namely Al_3Ni_2, Al_3Ni, and Al, by the profile refinement method. X-ray micro-tomography and optical microscopy were used to study the porosity formation inside the particles. It was found that for particles having sizes decreasing from 925 to 256 μm (increasing cooling rate), the weight fraction of Al_3Ni and eutectic Al decreases while that of Al_3Ni_2 increases. Furthermore, the droplets formed at higher cooling rates yielded a lower volume fraction of porosity.

Introduction

While a peritectic reaction during solidification is still not very well understood [1, 2], the aluminum rich side of the aluminum–nickel alloy system has two such reactions, which presents a significant challenge towards understanding and quantifying the solidification path of these alloys. Aluminum–nickel alloys are used as a heterogeneous catalyst in a variety of organic syntheses. The phase fractions of Al_3Ni_2, Al_3Ni, and Al formed during solidification have an important effect on the performance of these alloys in their applications. For example, Devred et al. [3] found that the catalytic activity of Raney Nickel ($Al_{68.5}Ni_{31.5}$) was very sensitive to initial alloy composition and increased with increasing fraction of Al_3Ni phase. It is, therefore, vital to know and to predict the phase fractions formed during the solidification of Al–Ni alloys under a range of cooling conditions.

Rapid solidification of materials can produce a refined microstructure, extension of solid solubility, change in morphology, and formation of metastable phases. With such significant advantages, many rapid solidification techniques have been used to study phase selection during solidification of Al–Ni alloys. Patchett and Abbaschian [4] studied the rapid solidification of Al-16.5 to 40.8 at.% Ni using splat cooling and drop tube experiments. They found that cooling rate can greatly alter the volume fractions of pro-peritectic, peritectic, and eutectic phases. Bao et al. [5] analyzed Al–Ni powders produced by gas atomization having different compositions on the Al-rich side of the phase diagram. They used neutron diffraction (ND) and X-ray diffraction (XRD) to identify the existing phases at the surface and in the bulk of the particles. Their results show a significant dependence of phase selection during the solidification of different sized gas atomized particles. Other scientists simulated the solidification of aluminum–nickel alloys using microsegregation [6] and phase field [7] models, and showed that there is a strong influence of cooling rate and temperature gradient on the solidification path of these alloys.

Although some papers have been published on this subject, the effect of rapid solidification conditions on the

A. Ilbagi (✉) · H. Henein
Department of Chemical and Materials Engineering, University of Alberta, Edmonton, AB T6G 2G6, Canada
e-mail: ilbagi@ualberta.ca

A. B. Phillion
School of Engineering, The University of British Columbia, Kelowna, BC V1V 1V7, Canada

resulting phase selection and the associated shrinkage porosity is still not well understood. In this paper, a relatively new technique called impulse atomization (IA) is used to generate rapidly solidified particles of $Al_{68.5}Ni_{31.5}$ alloy. The details of the technique can be found elsewhere [8, 9]; however, it is briefly discussed in the following section. The powders are then characterized using XRD, ND, scanning electron microscope (SEM), optical microscope (OM), and X-ray micro-tomography to measure the weight fractions of different phases and to investigate the porosity formation as a function of cooling rate.

Experimental

Powders of $Al_{68.5}Ni_{31.5}$ were produced by melting aluminum granules (99.9% pure) and nickel shot (99.9% pure) in an induction furnace under different atmospheres of helium and nitrogen. This composition is indicated by an arrow in Fig. 1 [10]. The IA was performed by holding the alloy at 100 °C above the liquidus temperature for 30 min. Then, the liquid was pushed through an orifice(s) at the bottom of the crucible to generate a liquid stream, which subsequently broke up into spherical droplets by Rayleigh instability [8]. The droplets lose their heat as they fall through a stagnant gas atmosphere of either helium or nitrogen having a maximum oxygen content of 10 ppm. The powders are solidified by the time they reach an oil quench bath at 4 m from the atomizing nozzle. The solidified droplets are subsequently washed and sieved into different sizes based on MPIF Standard 05 [11]. The actual composition of each alloy was measured using the ICP-AES technique.

Samples of different sized powders were mounted in epoxy and then ground and polished for microstructural analysis. SEM was performed using a Zeiss Evo MA15 to study the microstructure of the different sized particles and to measure the secondary dendrite arm spacing (SDAS). The mean distance between the dendrite arms was measured by performing 30 measurements on each particle size. EDX analysis on the SEM was done using a Bruker Silicon Drift Detector with a peak resolution of 125 eV.

In order to investigate the effect of processing parameters and particle size on the microsegregation of the solidified droplets, two diffraction methods were used. XRD was used to give an indication of the phase fractions close to the surface of the particles. However, to obtain the phase fractions from the bulk of the particles, ND was conducted on 328 and 780 μm particles. Experiments performed at the Oak Ridge National Laboratory (ORNL) in Oak Ridge, Tennessee, and Atomic Energy of Canada Limited (AECL) in Chalk River, Ontario. The ND experiment was conducted using a neutron beam of 1.33 Å wavelength. The XRD experiments on particles size ranging from 181 to 1200 μm were carried out using Kα radiation from Cu source on a Rigaku Denki Rotaflex RU-200B X-Ray generator at University of Alberta. To obtain the weight fraction of the phases formed under different conditions, Rietveld analysis was performed using the GSAS software [12].

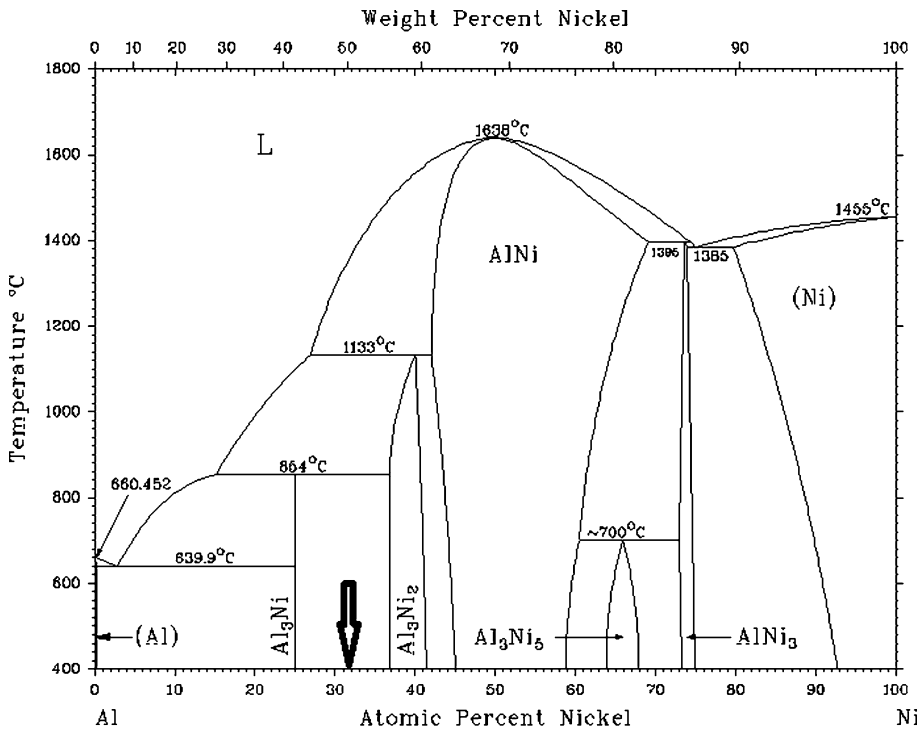

Fig. 1 Al–Ni phase diagram [8]. *Arrows* show the compositions investigated in this research

Optical microscopy using Leica DM ILM was utilized to investigate the porosity fraction within the cross-section of the particles. Image analysis on these images was performed using the ImageJ software. Further investigations on the amount and distribution of porosity were conducted using X-ray micro-tomography on the droplets of diameter of 181 and 328 μm. The experiments were carried out on the ID19 beam line at the European Synchrotron Radiation Facility (ESRF) in Grenoble, France (0.28 μm resolution) and on the beam line Tomcat, X02DA at Swiss Light Source, Paul Scherrer Institut, Villigen, Switzerland (0.37 μm resolution). Quantitative analysis of this data required a tedious and memory intensive pre-processing to remove background noise and X-ray artifacts. The method used to ease this process is explained in detail elsewhere [13]. In brief, a clean mask file of the droplet was generated using MATLAB image toolbox and then applied to the original data to eliminate all but the structural features of interest. High performance visualization software, Avizo®, was then used to visualize the porosity distribution within the droplets.

Results

Table 1 shows the conditions of specific IA runs, as well as the actual composition of the particles measured using ICP-AES technique. The mass mean droplet diameter (D_{50}) and the log-normal standard deviation (σ) were calculated from the powder size distribution fitted to a log-normal function.

SEM

The effect of cooling gas and particle size on the scale of microstructure was investigated. In brief, microstructural analysis of the produced particles using SEM showed that the particles have almost perfect spherical shape with an internal dendritic microstructure, the size of which is dependent on the cooling rate. Figure 2 shows an example of the effect of cooling gas, where using helium (a) as oppose to nitrogen (b) resulted in a refined microstructure for particles of the same size. Both micrographs seem to have a typical peritectic structure, in which the light gray phase is surrounded by dark gray phase. EDX analysis showed that the dark gray phase contain 24 at% nickel, which can be attributed to Al_3Ni, while the core of the dendrites has 42 at% nickel, close to that of Al_3Ni_2. The area between the dendrites is the non-equilibrium eutectic, shown as the black phase and contains more than 96 at% aluminum. An interesting point is the morphology of the dark gray phase in Fig. 2b that apparently, grew freely into the liquid.

Besides changing the type of the cooling gas, decreasing the particle size was also found to affect the microstructure of the atomized particles. This is evident from the changes

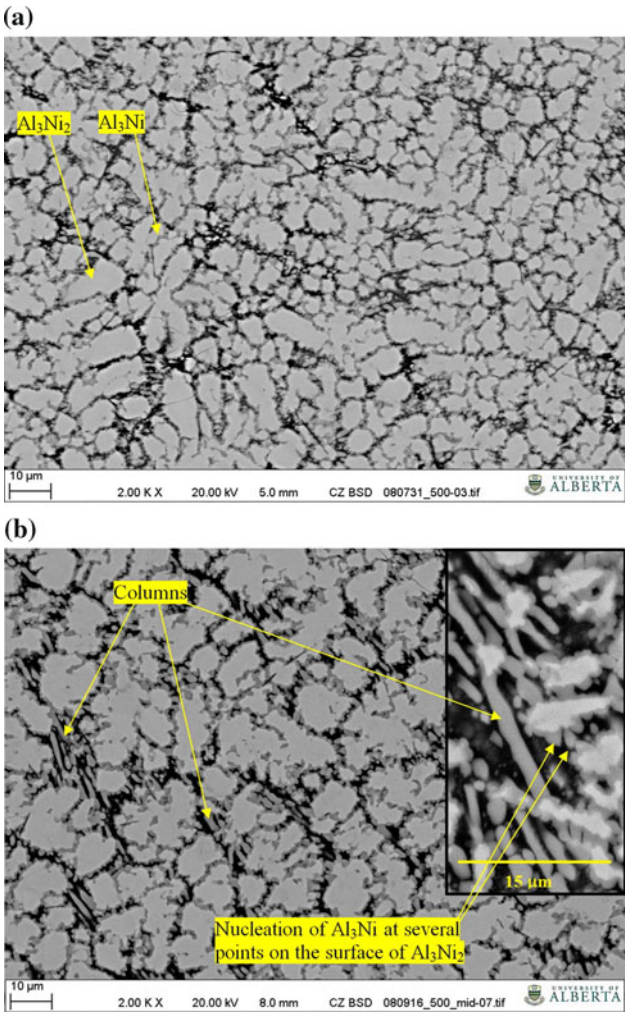

Fig. 2 Microstructure of atomized particle of $Al_{68.5}Ni_{31.5}$, **a** atomized in helium **b** atomized in nitrogen. Diameter of both particles is 550 μm

Table 1 Alloy compositions and atomization conditions

Atomization run number	Atomization atmosphere	Nominal composition	Number of orifices	Actual composition	D_{50}/σ^a
080731	He	$Al_{68.5}Ni_{31.5}$	37	Al–31.3 at% Ni	436/1.46
080916	N_2	$Al_{68.5}Ni_{31.5}$	37	Al–31.1 at% Ni	402/1.39

[a] $\sigma = D_{84}/D_{50}$

Table 2 The effect of particle size and cooling gas on the SDAS

Particle size	Average SDAS (μm)/expected cooling rate (°C/s)	
	Atomized in He	Atomized in N_2
181	2.48 ± 0.12/28000	4.16 ± 0.20/6000
328	4.21 ± 0.30/5700	6.04 ± 0.31/1900
550	5.36 ± 0.24/2800	8.19 ± 0.28/800
925	8.53 ± 0.15/700	10.66 ± 0.27/300

Table 3 Values used to calculate the cooling rate of atomized particles

Name	Symbol	Value	Unit
Diffusion coefficient	D	10^{-8}	m^2s^{-1}
Gibbs–Thomson coefficient	Γ	10^{-8}	mK

in the SDAS values. Table 2 lists the SDAS as a function of particle size in both helium and nitrogen. Also, using the data listed in Table 3 and the equilibrium phase diagram, the cooling rates of the particles were calculated and shown in Table 2. Details of this calculation are discussed in "Discussion" section.

XRD and ND

Rietveld analysis was carried out using GSAS on both ND and XRD data from different particle sizes atomized in helium and nitrogen. Figure 3 shows one example of the measured XRD pattern of $Al_{68.5}Ni_{31.5}$ with the diameter of

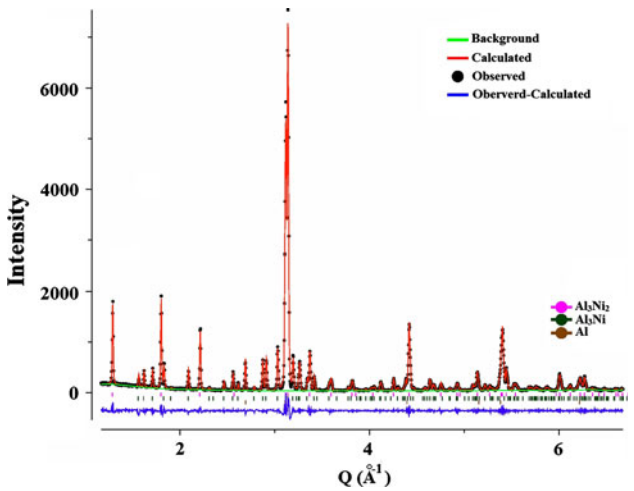

Fig. 3 Profile refinement of $Al_{68.5}Ni_{31.5}$ with the diameter of 390 μm and cooled in nitrogen using the GSAS computer code. The *top line* shows the calculated diffraction pattern as obtained from GSAS software and the *bottom line* represents the difference between the observed and calculated diffraction pattern. The *small vertical bars* indicate the positions of diffraction peaks of the Al_3Ni_2 (*top*), Al_3Ni (*middle*), and Al (*below*)

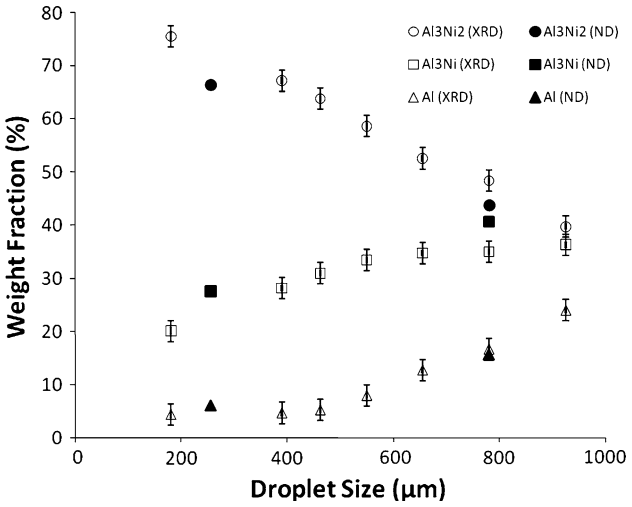

Fig. 4 Weight fraction of Al_3Ni_2 (*circles*), Al_3Ni (*squares*), and Al (*triangles*) as a function of droplet size of $Al_{68.5}Ni_{31.5}$ atomized in nitrogen

390 μm and cooled in nitrogen. A profile refinement using the GSAS computer code showed that only three phases (i.e., Al_3Ni_2, Al_3Ni, and Al) existed in the entire size range (256, 390, 463, 550, 780, 925 μm) that was investigated. In Fig. 3, the top line shows the calculated diffraction pattern as obtained from GSAS software and the bottom line represents the difference between the observed and calculated diffraction pattern. The small vertical bars indicate the positions of diffraction peaks of the Al_3Ni_2 (top), Al_3Ni (middle), and Al (below). Figure 4 shows the weight fraction of the phases formed in the particles of $Al_{68.5}Ni_{31.5}$ atomized in nitrogen. It can be seen that with increasing particle size, the weight fraction of Al_3Ni_2 (circles) decreases while the weight fraction of Al_3Ni (squares) increases. Al follows the same trend as Al_3Ni, which is the direct result of increasing eutectic fraction as particle size increases. This increase in the amount of Al is more strongly dependent on particle size for the sample atomized in nitrogen as compared to those of atomized in helium (Fig. 5). It is also clear that at smaller particle sizes, both helium and nitrogen resulted in almost same amount of eutectic phase.

Figure 6 shows the ratio of Al_3Ni/Al_3Ni_2 as a function of droplet size in $Al_{68.5}Ni_{31.5}$. Empty symbols are from the sample atomized in nitrogen and full symbols are from the sample atomized in helium. Circles and squares represent XRD and ND data, respectively. It is obvious that the fraction of Al_3Ni increases as the cooling rate decreased (larger particles), and this effect is more pronounced in nitrogen-cooled samples while the helium-cooled samples do not significantly increase for sizes greater than 400 μm. This will be further analyzed in "Discussion" section.

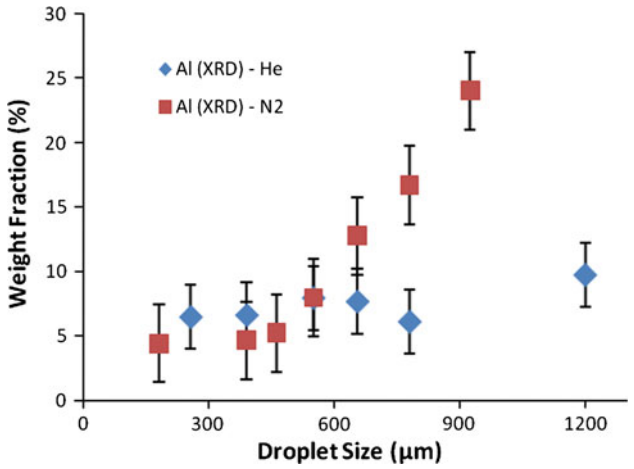

Fig. 5 Comparison of the weight fraction of Al versus droplet size for the $Al_{68.5}Ni_{31.5}$ sample atomized in helium and in nitrogen

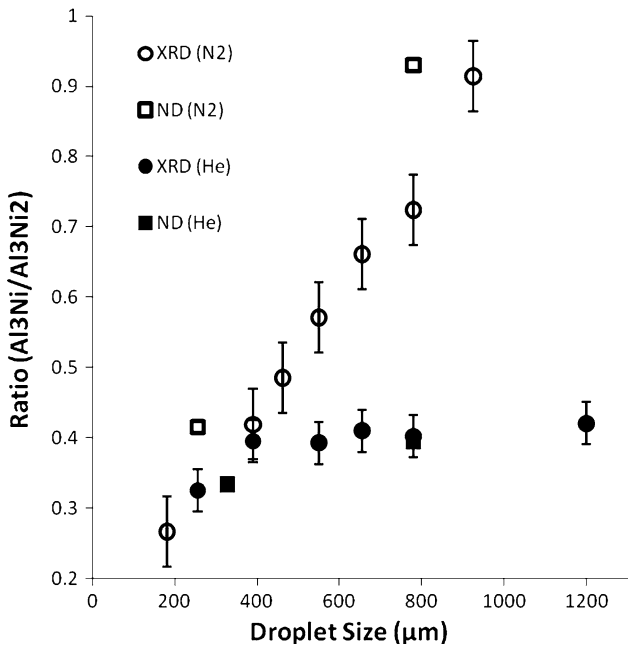

Fig. 6 Ratio of Al_3Ni/Al_3Ni_2 as a function of droplet size in $Al_{68.5}Ni_{31.5}$

Optical microscopy and X-ray micro-tomography

Optical images of more than 30 particles from each of different sizes were analyzed using the image processing software called ImageJ. Since the images were high contrast, and the porosity appeared black, the measurement of the porosity within each particle was straightforward. Figure 7 shows sample cross-sections of particles having 181 and 925 μm diameters of $Al_{68.5}Ni_{31.5}$, atomized in helium. It seems that in larger particles (lower cooling rates) the distribution of porosity is different than that of smaller particles. In smaller particles, such as in Fig. 7a,

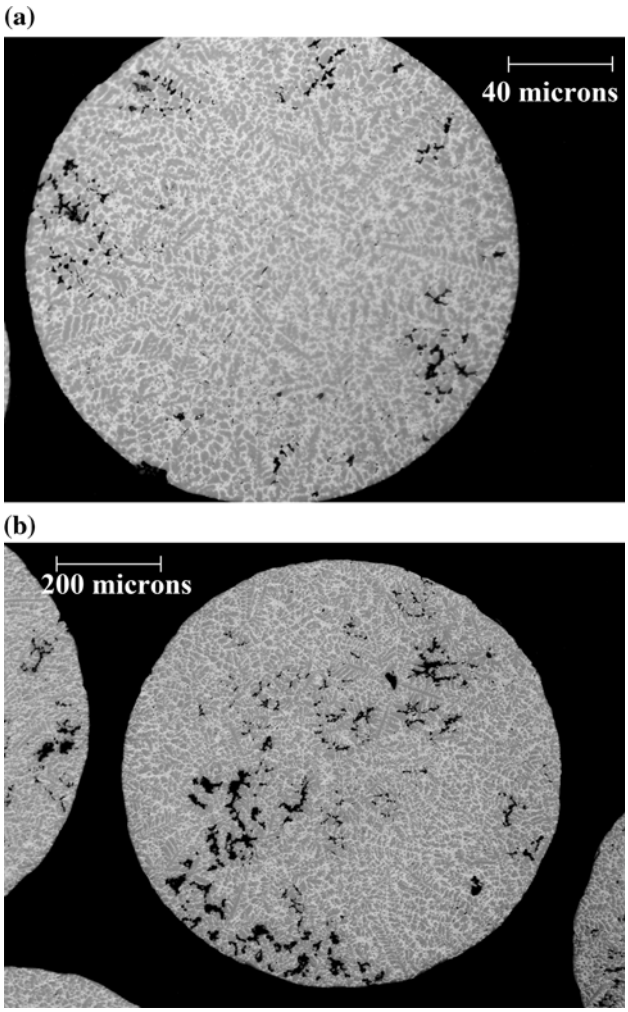

Fig. 7 Optical microscopy images of $Al_{68.5}Ni_{31.5}$ particles atomized in helium. **a** 181 μm, **b** 925 μm

181 μm diameter, porosity tends to form closer to the periphery of the particle, whereas in larger particles, 925 μm diameter (Fig. 7b), the pores are more randomly distributed. Also, as the microstructure is refined due to higher cooling rate, the size of the individual pores decreases. Figure 8 shows the variation of the area fraction of porosity in $Al_{68.5}Ni_{31.5}$ atomized in helium and nitrogen as a function of particle size. From these images it seems that the fraction of porosity increases with decreasing cooling rate. However, 2-D methods are limited by the small number of sections that can be viewed for a given sample. Also, since the intermetallics are quite brittle, not all porosity may be due to solidification shrinkage. Some may result from material loss during sample preparation. Therefore, a 3-D method has obvious advantages over conventional 2-D approaches. X-ray micro-tomography was used to gather 3-D information on rapidly solidified atomized Al-Ni droplets. From the analysis performed on X-ray micro-tomography images, similar trend to what was

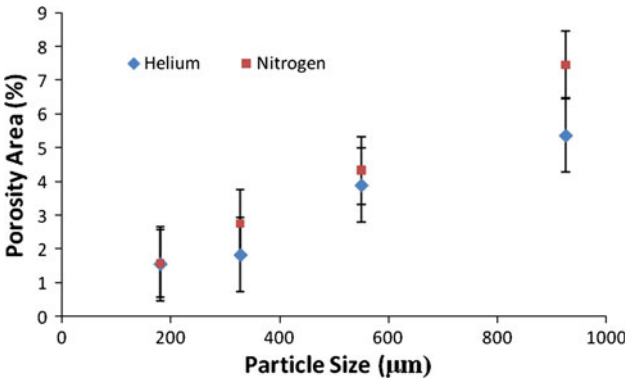

Fig. 8 Variation of area fraction of porosity in different particle sizes of $Al_{68.5}Ni_{31.5}$ atomized in helium and nitrogen

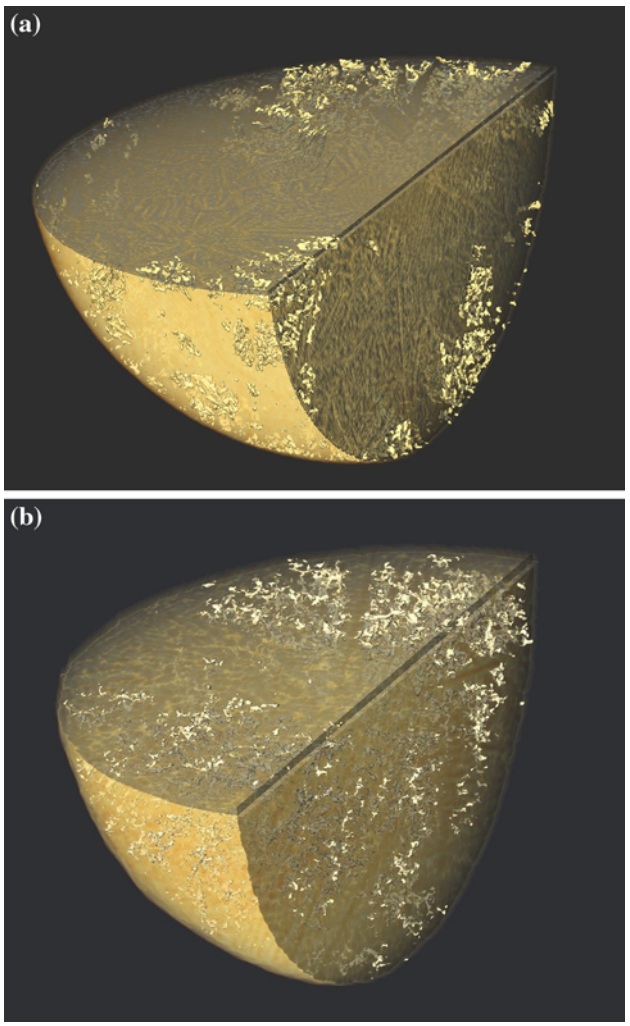

Fig. 9 Visualization of the porosity within two particles of 328 μm diameter, atomized in helium (**a**) and nitrogen (**b**)

found using optical microscope was observed. Specifically, porosity tends to form closer to the periphery in droplets cooled in helium compared with those cooled in nitrogen,

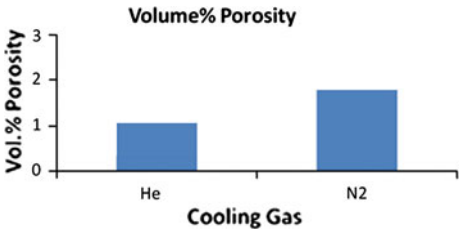

Fig. 10 Quantification of porosity resulted from image analysis on X-ray micro-tomography data of 328 μm diameter droplet showing the effect of cooling gas, helium versus nitrogen

as is visualized in Fig. 9. In this figure, two 328 μm diameter particles are shown. The particle in Fig. 9a was atomized in helium while the particle in Fig. 9b was atomized in nitrogen. Quantitative analysis of these images revealed that the volume percent of the porosity decreases if helium is used instead of nitrogen. Figure 10 shows the result of such analysis. The volume percent of the porosity measured from this method follows the same trend as that of Fig. 8.

Discussion

Effect of cooling rate on microstructure and phase selection

Dendrite arm spacing can be related to cooling rate according to Eq. 1 [14],

$$\lambda = B\dot{T}^{-n} \tag{1}$$

where λ (μm) represents the dendrite arm spacing, $\dot{T}$ (°C/s) is the cooling rate during solidification, B (μm(°C/s)^n), and n (dimensionless) are constant. These constants are derived empirically by comparing the dendrite arm spacing to the cooling rate. Unfortunately, these constants have not been reported for $Al_{68.5}Ni_{31.5}$. Therefore, in order to estimate the cooling rate in this experiment another approach was taken.

Secondary dendrite arm spacing is a function of the extent of coarsening that occurs during solidification as it was shown by Kurz and Fisher [15]. They showed that the spacing between the arms is proportional to the cube of time (t).

$$\lambda = 5.5\,(Mt)^{\frac{1}{3}} \tag{2}$$

With

$$M = \frac{\Gamma D \ln\left(\frac{C_1^m}{C_0}\right)}{m(1-k)\left(C_0 - C_1^m\right)} \tag{3}$$

where Γ is the Gibbs–Thompson coefficient, D is the diffusion coefficient of solute in the liquid, m is the slope of the liquidus line, C_1^m is the composition of the last liquid to

solidify, and C_0 is the overall composition. Except for Γ and D, the rest of the parameters can be found from the phase diagram. In the case of $Al_{68.5}Ni_{31.5}$, it was assumed that the liquidus line is linear, and the dendrite arm coarsening has generally occurred before the first peritectic reaction takes place. The role of diffusion coefficient in the coarsening of dendrites is crucial; however, at this point, experimental data for $Al_{68.5}Ni_{31.5}$ is lacking. Therefore, the values suggested by Tourret and Gandin [6] (Table 3) were used.

The results show that increasing cooling rate as a result of decreasing particle size, or using helium instead of nitrogen, refines the microstructure, as it seen in Table 2. This is also evident in Fig. 2. Since the thermal conductivity of helium is significantly higher than that of nitrogen [16] this was an expected outcome.

One interesting point of Fig. 2 is the morphology of the Al_3Ni phase. This figure shows that Al_3Ni does not completely envelop Al_3Ni_2. Rather, nucleation of Al_3Ni occurs at several points on the surface of Al_3Ni_2 dendrites (Fig. 2b). This was also observed by Patchett and Abbaschian [4]. This is in contrast to the conventional understanding of peritectic formation, in which the formation of an envelope of the peritectic phase around the primary phase immediately after its nucleation is assumed [17]. In the case of Al–Ni alloys, this special type of peritectic phase nucleation and the observation of eutectic in the intergranular region leads to this conclusion that a three phase contact between liquid and two solids remains throughout solidification prior to eutectic formation. This results in enhanced dissolution of the primary phase. Increasing the cooling rate and thus, decreasing secondary dendrite arm spacing, reduces the space for the three phase contact faster, as the gap between the arms is filled by the peritectic product. As a result, less dissolution of the primary phase occurs. This can explain the trend observed in Fig. 3, where the weight fraction of the Al_3Ni_2 increases with decreasing particle size. Similar trends were observed by Bao et al. [5] and predicted by Tourret and Gandin [6].

St John and Hogan [18] proposed that the rate at which a peritectic reaction goes to completion is directly related to the shape of the peritectic region on the phase diagram. In the case of Al_3Ni, having an exact stoichiometric composition eliminates the strong influence of a composition gradient within the peritectic product. As a result, the rate of transformation becomes extremely slow. Since the peritectic reaction is a time dependant process, this complication causes a reduction of the peritectic product at higher cooling rates, which is observed in both Figs. 4 and 6.

While the weight fraction of Al_3Ni_2 increases with increasing cooling rate, the weight fraction of Al, the eutectic product, is reduced. This same trend was reported by Kasperovich et al. [19] in eutectic alloys, in which the eutectic fraction increased with decreasing cooling rate. Also, Patchett and Abbaschian [4] showed the same trend as that of Fig. 5. However, Bao et al. [5] reported that the eutectic fraction increased at higher cooling rate in gas atomized particles. Also, Tourret and Gandin [6] predicted similar dependence of the eutectic fraction to cooling rate during the solidification of particles that were generally much smaller than those studied in this paper. The reason for this scatter is the fact that the fraction of the non-equilibrium eutectic is a function of the processing parameters, i.e., the cooling rate and the solidification rate. This was shown by Sarreal and Abbaschian [20] in Al–Cu and Al–Si. They argued that when the cooling rate increases, the dendrite tip undercooling and also, eutectic undercooling are responsible for the decrease in the fraction of eutectic. More research is required to justify the trends observed in the impulse atomized droplets of Al–Ni alloy.

One other interesting feature seen in Fig. 4 is that the weight fraction of the Al_3Ni_2 measured by ND is slightly less than that of XRD. While it is an expected result, considering that the data in ND comes from the entire particle, the small difference between XRD and ND results, as compared with that of gas atomized particles [5], can prove the fact that the particles in IA have very small internal temperature gradients. This was previously assumed by Wiskel et al. [9]. This also indicates that Ni–Al IA particles may be more homogeneous in structure than gas atomized particles or than Al–Cu IA [21] and Al–Fe IA [22] powders. More ND on different particles sizes is required to further confirm these results.

Effect of phase selection on porosity formation

Growth of Al_3Ni results in narrower feeding channels for the liquid. This is because Al_3Ni forms around the primary dendrite, Al_3Ni_2, which itself has experienced a relatively long solidification interval. Also, as it is observed in Fig. 2b, after nucleation occurs as a result of peritectic reaction, the Al_3Ni grows freely into the liquid when the cooling rate decreases, which results in completely isolating the liquid in the inter-dendritic region. Since the dendrite arm spacing is larger at lower cooling rates, the size of individual porosity also increases, as illustrated in Fig. 7.

It is a common belief that as the fraction of eutectic liquid increases, the feeding path becomes wider and feeding becomes easier [23]. That is not the case in this alloy, however. Although the fraction of the Al, and hence, the liquid increases when the cooling rate decreases (see Fig. 5), the volume percent of porosity has increased (Fig. 8). Once again, this is a result of the growth of long columns of Al_3Ni, which isolates larger amount of liquid in the inter-dendritic region.

Using micro-tomography has the advantage of providing 3-D data in a non-destructive manner. The result of micro-tomography not only helped measure the amount of porosity within particles, but it also allowed for visualizing the distribution of porosity inside the particles by using the image processing technique mentioned in the previous section. From this analysis it was found that both volume percent porosity as well as porosity distribution vary with the cooling rate (Figs. 9 and 10). The quantitative analysis of the images taken using this method is in agreement with the previous results obtained from OM. It seems that in the range of cooling rates that the particles of $Al_{68.5}Ni_{31.5}$ experienced during IA, volume percent of porosity is directly related to the weight fraction of Al_3Ni.

Summary

$Al_{68.5}Ni_{31.5}$ was atomized in stagnant helium and nitrogen using the IA technique. A finer microstructure was achieved in the smaller particle sizes. Using helium instead of nitrogen also resulted in a refined microstructure. Rietveld analysis on ND and XRD data of the particles studied showed that only three phases (i.e., Al_3Ni_2, Al_3Ni, and Al) formed in the entire size range (256, 390, 463, 550, 780, 925 μm) that was investigated.

Increasing the cooling rate decreased the weight fraction of Al_3Ni and Al. However, it increased the weight fraction of Al_3Ni_2.

Optical microscopy and X-ray micro-tomography were used to investigate the effect of cooling rate on the formation of the porosity. It was found that in smaller particles, porosity tends to form closer to the periphery of the particles, whereas in larger particles the pores are more randomly distributed.

At lower cooling rate Al_3Ni seems to grow freely into the melt. This can isolate the liquid in the inter-dendritic region, which causes more porosity.

Acknowledgements This research was supported by Canadian Space Agency (CSA) and by Natural Sciences and Engineering Research Council of Canada (NSERC). The authors would like to thank Atomic Energy Canada Limited (AECL), Chalk River, and Oak Ridge National Laboratory (ORNL), TN, USA, for their support in conducting the neutron diffraction experiments. We would also like to acknowledge The Swiss Light Source, Paul Scherrer Institut, Villigen, Switzerland, and European Synchrotron Radiation Facility (ESRF) in Grenoble, France for beam time. The authors are grateful to Guillaume Reinhart for conducting micro-tomography experiments. We are also thankful to Ian Swainson, Ulf Dahlborg and Monique Calvo-Dahlborg for their assistance in data analysis.

References

1. Sumida M (2003) J Alloy Compd 349(1–2):302
2. Liu Y, Lan F, Yang G, Zhou Y (2004) J Cryst Growth 271(1–2): 313
3. Devred F, Gieske AH, Adkins N, Dahlborg U, Bao CM, Calvo-Dahlborg M, Bakker JW, Nieuwenhuys BE (2009) Appl Catal A Gen 356(2):154
4. Patchett JA, Abbaschian GJ (1986) In: Mehrabian R, Parrish PA (eds) Proceeding of the fourth conference on rapid solidification processing: principles and technologies. University of California, Santa Barbara, CA, USA
5. Bao CM, Dahlborga U, Adkinsb N, Calvo-Dahlborg M (2009) J Alloy Compd 481:199
6. Tourret D, Gandin Ch-A (2009) Acta Mater 57:2066
7. Siquieri R, Doernberg E, Emmerich H, Schmid-Fetzer R (2009) J Phys 21:464112 (6 pp)
8. Henein H (2002) Mater Sci Eng A 326(1):92
9. Wiskel JB, Henein H, Maire E (2002) Canadian Metall Q 41(1):97
10. Nash P, Singleton MF, Murray JL (1991) Phase diagrams of binary nickel alloys. ASM, Materials Park, OH, p 3
11. Standard test methods for metal powders and powder metallurgy products, Metal Powder Industries Federation, Princeton, NJ (1993)
12. Von Dreele RB (1994) Neutron diffraction in materials science and technology: a comprehensive treatment, vol 2B. Wiley–VCHl, New York, NY
13. Johansson J, Ilbagi A, Thornton D, Henein H (2010) Processing 3D data sets from X-ray tomography of impulse atomized metal particles. TMS Annual Meeting, Seattle, WA, USA
14. Jones H (1983) Rapid solidification of metals and alloys. The Institution of Metallurgists, London, p 40
15. Kurz W, Fisher DJ (1989) Fundamentals of solidification. Transaction Technical Publication, Switzerland, p 88
16. Rohsenow WM, Hartnett JP, Cho YI (1998) Handbook of heat transfer, 3rd edn. McGraw-Hill, New York
17. Kerr HW, Cisse J, Bolling GF (1974) Acta Metall 22:677
18. St John DH, Hogan LM (1987) Acta Metall 35(1):171
19. Kasperovich G, Volmann T, Ratke L, Herlach D (2008) Metall Mater Trans A 39(5):1183
20. Sarreal J, Abbaschian G (1986) Metall Mater Trans A 17(11): 2063
21. Prasad A (2006) Microsegregation studies of rapidly solidified binary Al–Cu alloys. PhD Thesis, University of Alberta
22. Buchoud V, Schmidt R-R, Henein H, Malahof D, Gandin C-A, Lesoult G, Uhlenwinkle V (2010) Canadian Metall Q 49(3):275
23. Han Q (2008) Shrinkage porosity and gas porosity, casting, vol 15, ASM handbook. ASM International, Ohio, p 370